The feasibility of non-contact ultrasound for medical imaging

2013 Phys. Med. Biol. 58 6263

(http://iopscience.iop.org/0031-9155/58/18/6263)

IOP PUBLISHING PHYSICS IN MEDICINE AND BIOLOGY

Phys. Med. Biol. **58** (2013) 6263–6278 doi:10.1088/0031-9155/58/18/6263

The feasibility of non-contact ultrasound for medical imaging

G T Clement[1], H Nomura[2], H Adachi[1] and T Kamakura[2]

[1] Center for Industrial and Government Relations, The University of Electro-Communications, 1-5-1 Chofugaoka, Chofu-shi, Tokyo 182-8585, Japan
[2] Graduate School of Informatics and Engineering, The University of Electro-Communications, 1-5-1 Chofugaoka, Chofu-shi, Tokyo 182-8585, Japan

E-mail: gclement@physics.org

Received 15 April 2013, in final form 21 June 2013
Published 22 August 2013
Online at stacks.iop.org/PMB/58/6263

Abstract

High intensity focused ultrasound in air may provide a means for medical and biological imaging without direct coupling of an ultrasound probe. In this study, an approach based on highly focused ultrasound in air is described and the feasibility of the technique is assessed. The overall method is based on the observations that (1) ultrasound in air has superior focusing ability and stronger nonlinear harmonic generation as compared to tissue propagation and (2) a tightly focused field directed into tissue causes point-like spreading that may be regarded as a source for generalized diffraction tomography. Simulations of a spherically-curved transducer are performed, where the transducer's radiation pattern is directed from air into tissue. It is predicted that a focal pressure of 162 dB (2.5 kPa) is sufficient to direct ultrasound through the body, and provide a small but measurable signal (∼1 mPa) upon exit. Based on the simulations, a 20 cm diameter array consisting of 298 transducers is constructed. For this feasibility study, a 40 kHz resonance frequency is selected based on the commercial availability of such transducers. The array is used to focus through water and acrylic phantoms, and the time history of the exiting signal is evaluated. Sufficient data are acquired to demonstrate a low-resolution tomographic reconstruction. Finally, to demonstrate the feasibility to record a signal *in vivo*, a 75 mm × 55 mm section of a human hand is imaged in a C-mode configuration.

(Some figures may appear in colour only in the online journal)

1. Introduction

A clear limitation of ultrasound, as compared to other widely used medical imaging modalities (e.g. MRI, CT, x-ray, and PET) is the need to place the patient in direct contact with the device. Good ultrasound coupling is critical, typically requiring operation by a skilled sonographer.

Such coupling can also be particularly problematic in emergency and surgical situations where sterile conditions must be maintained or where contact with the skin is restricted.

While ultrasound could theoretically be transmitted from air into tissue, the enormous impedance mismatch at this interface prevents nearly all passage of ultrasound into—and out of—the body. As such, this approach has widely been regarded as unattainable. In nondestructive testing (NDT), ultrasound signals from air through solid materials can be achieved (Gan *et al* 2001); however these signals consist of a complex summation of multiple reflections within the object itself (Berriman *et al* 2005). This signal is further complicated by the induction of shear modes of vibration within solid structures and contributions from modes of vibration along the surface of the material. Such signals have found value in certain industrial applications where the goal is to identify bulk properties across the thickness of a surface, or to find defects in thin and otherwise regular materials. Similar techniques have demonstrated feasibility for medical application (Iraniha *et al* 2000, Bulman *et al* 2012), including the recent formation of transmittance maps over bone phantom surfaces (Bulman *et al* 2012).

Tomographic reconstruction, however, requires the detection and interpretation of scattering due to internal structure. The relevant signal must consist of the isolated first-order longitudinal scattering from these structural variations. This signal has been achieved in NDT for the purpose of ray-based sensing (Gan *et al* 2002, Hall 2011) where signal encoding and long term averaging was used to determine the time of first arrival of the longitudinal modes of vibration through materials. In these works, the detection of embedded objects was demonstrated, but at resolutions far lower than those achievable with wave-based image reconstruction.

To evaluate the potential to perform wave based tomographic reconstruction via an air-coupled (i.e., *non-contact*) approach, we presently investigate three key challenges: the ability to transmit a coherent signal into tissue, the ability to receive a waveform exiting tissue, and the potential to interpret this signal for image reconstruction. Our approach to each of these challenges is addressed through the use of a high intensity focused source in air.

It is expected that air's lower sound speed as compared to tissues will allow a focal diameter more than four times smaller than that attainable by the same signal in tissue, while at the same time inducing nonlinear generation of signal harmonics. It is hypothesized that a highly focused radiator can be constructed that can produce a focal intensity of sufficient intensity to allow detection of waves, even after exiting tissue. It is further hypothesized that for a sufficiently small focus, the point of entry into the tissue can be regarded as a point source, permitting an image to be formed via fan-beam diffraction tomography (Devaney 1985); albeit a generalized tomography (Devaney 1982) where the source points of the *fan* lie on the (generally irregular (Devaney and Beylkin 1984)) boundary of the object itself. The following work tests of these hypotheses and quantifies the parameters necessary for future development.

2. Methods

2.1. Simulation

Preliminary simulations modeled ultrasound propagation through an air–water–air three layer system, the water being used as a generic approximation for tissue. The purpose of the simulation was to assess the ability to create a focus in air much smaller than the signal's wavelength in water, and to assess the amplitude and shape of the waveform within the layer and upon exiting the layer. Pressure field modeling was performed using a linearized pseudospectral wavevector-frequency domain approach to the inhomogeneous wave equation (Jing *et al* 2012, Treeby *et al* 2012). The algorithm was implemented by specifying the time

history of an initial incoming wave propagating forward through the boundary of a Cartesian volume of known density $\rho(\mathbf{r})$, absorption $\alpha_f(\mathbf{r})$ and sound speed $c(\mathbf{r})$. In the present study, this initial wave was fully contained within a single surface of the volume. A key feature of the approach is the ability to measure scattering to an arbitrary order. In the present case, scattering up to the fourth order was considered. While higher-order scattering for this highly-mismatched situation is to be expected, only the initially-exiting waves coming from these initial reflections is relevant to the present analysis.

A 180 mm diameter focused transducer with a 160 mm radius of curvature was modeled at 40 and 80 kHz. The frequencies were selected due to the wide commercial availability of 40 kHz air ultrasound emitters, 80 kHz being the second harmonic. A 150 mm water layer ($\rho = 1000$ kg m^{-3}, $c = 1500$ m s^{-1}, $\alpha = 0.00$ Np m^{-1}) situated between two air layers ($\rho = 1.0$ kg m^{-3}, c $= 346$ m s^{-1} $\alpha_{40\,\mathrm{kHz}} = 0.07$ Np m^{-1}, $\alpha_{80\,\mathrm{kHz}} = 0.14$ Np m^{-1}) was simulated assuming radial symmetry over $z = 340$ mm $\times$ $\mathbf{r} = 125$ mm along the axes parallel and orthogonal to the transducer axis of symmetry, respectively, at a resolution of 0.5 mm $\times$ 0.4 mm, with the complex pressure simulated at all points over this grid.

2.2. Transducer

2.2.1. Design. With the intent of focusing via a spherically-curved array, simulations were carried out to optimize transducer parameters. A wavevector-frequency domain approach (Jing *et al* 2011) was used in this parametric study, which varied the diameter and radius of curvature of a spherically-curved surface consisting of circular 1 cm diameter, 40 kHz air ultrasound transducers. The goal of this design was to find the minimum surface area that would achieve a focal size of under 5 mm and a peak focal pressure of at least 2.5 kPa.

Transducer diameters of 150, 200, 250 and 300 mm were considered. For each diameter, D, the radius of curvature, ROC, was varied from D/2 to 1.5 D. Based on past work with the 40 kHz transducers selected for the present study, it was assumed that a peak surface pressure of approximately 80 Pa (129 dB) could be achieved at the peak voltage input rating of the elements (30 V). Simulated transducer geometries indicated that a 175 mm diameter, 90 mm ROC transducer could achieve a 40 $\times$ (32 dB) gain, resulting in a predicted focal peak of approximately 3.2 kPa with a full-width at half-maxima (FWHM) of approximately 5 mm (figure 1).

2.2.2. Construction. Four hundred high-Q ultrasound elements were acquired and individually tested for frequency response using a calibrated receiver. By way of this testing, an optimal driving frequency of 41.05 kHz was determined, and the 298 elements most closely matching this resonance value were selected for the array. These elements were affixed to a custom acrylic hemisphere, which was drilled to accommodate the leads of the individual elements while providing structural support. The array was constructed as a configuration of 11 concentric rings to allow for future axial steering capability, however, the rings were operated as a single transducer in the present study. The completed array is shown in figure 2.

2.2.3. Characterization. The peak pressure amplitude of the array was measured using a 3.18 mm diameter broadband microphone (Brüel & Kjær Model 4138, Nærum, Denmark), and amplifier (Brüel & Kjær Nexus) which were calibrated at 250 Hz using a pistophone (Brüel & Kjær Model 4220) prior to measurement. The calibration curve of the microphone was then used to determine the expected response at 41 kHz, which is well-within the specified operational range of the microphone (6 Hz to 140 kHz).

The transducer focus was determined by affixing the microphone to a positioning table (Proxxon KT 70) and manually finding the focal point of the transducer based on maximum

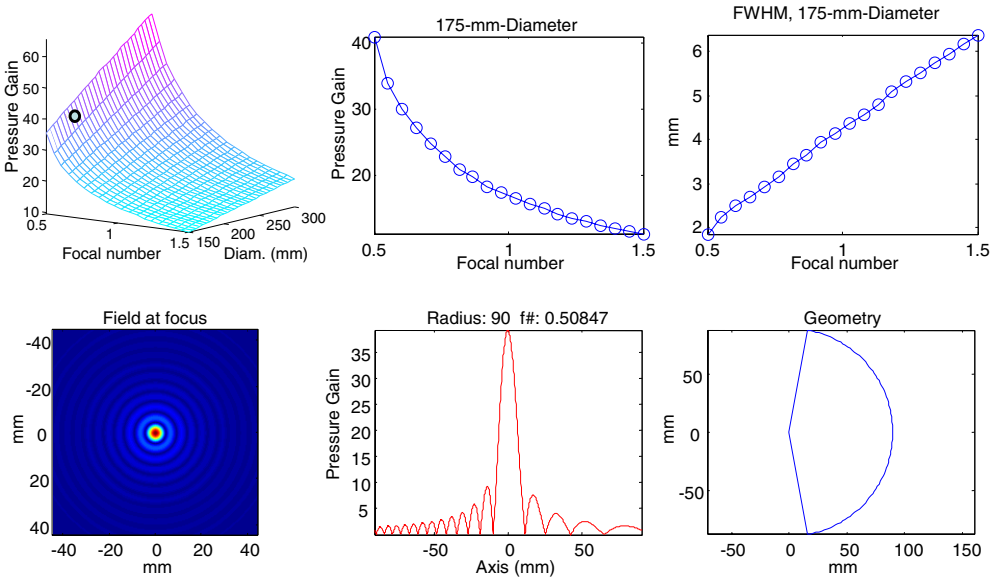

Figure 1. Array design sought a geometry that could focus within 5 mm in the radial plane and create a peak pressure of greater than 2.5 kPa. The selected focal number (0.51) and diameter (175 mm) are highlighted versus pressure gain (upper right smf center) and focal full-width at half-maxima (upper left). Transducer geometry and predicted beam profiles are illustrated in the lower plots.

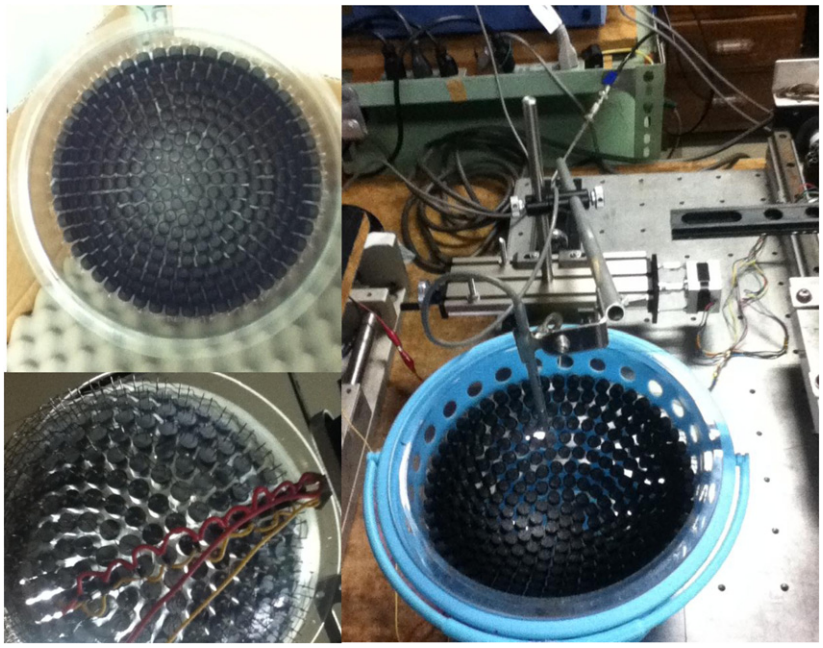

Figure 2. Images of the completed array showing a top view (upper left), the back of the array (lower left), and the array during characterization (right).

voltage of the received signal using a 30-cycle burst signal generated with an arbitrary waveform generator (NF 1966, Yokohama, Japan) and power amplifier (NF HSA 4015,

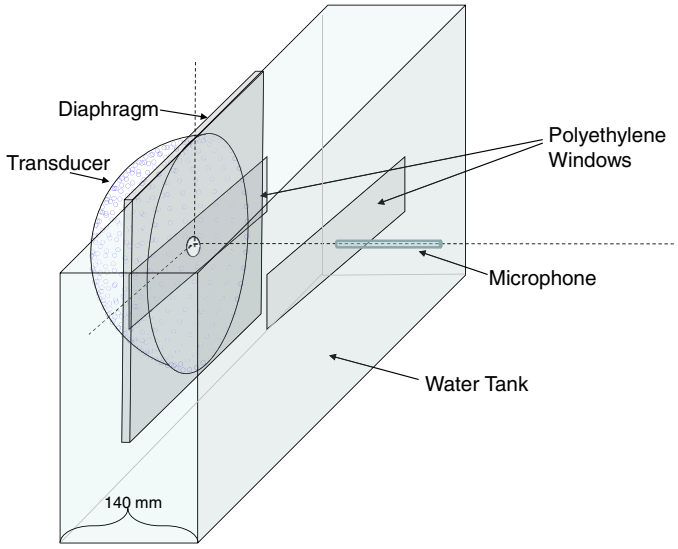

Figure 3. Schematic of the water phantom measurements. Both the microphone and transducer were affixed to linear positioners, with the transducer focal point situated upon the polyethylene surface of the water phantom.

Yokohama, Japan). The maximum voltage response from the calibrated microphone was measured with an oscilloscope (LeCroy Waverunner 6051 A, Chestnut Ridge, NY) while driving the transducer at 30 V, the maximum manufacturer rating of the elements.

Transducer beam profiles were performed using a stepping motor system (bipolar motors and double-h-bridge driver, built in-house) retrofitted to the Proxxon positioning table and controlled using eight digital outputs of a data acquisition device (DAQ) (X-Series 6366, National Instruments, Austin, TX). The 3.18 mm diameter microphone was scanned over a 40 mm $\times$ 40 mm area normal to the transducer axis of symmetry at a spatial step size of 1 mm. Transducer voltage was supplied from an analog output of the DAQ matched to 50 W and fed into an amplifier (NF HSA 4015). The output was a 30 V, 41.05 kHz 7-cycle sinusoidal burst. At each scan point the voltage amplitude from the microphone was acquired (DAQ analog input) and phases were determined by Fourier transform at the first, second, and third harmonics of the driving frequency. All signal generation, control, and acquisition software was written in-house utilizing the NI DAQ C-library externally called from Matlab (Mathworks, Inc., Natick, MA).

2.3. Phantom tests

A water phantom was utilized to assess the ability to measure a signal through tissue-like structures and to assess whether the first-order longitudinal signal passing through these materials could be separated from higher-order reflections within the phantoms, surface modes of vibration, and signals occurring external to the object. To create the phantom, a polyethylene bag (320 mm $\times$ 380 mm) was inserted into a 240 mm length $\times$ 140 mm width $\times$ 350 mm height plastic container and filled with water. The container was used for structural support had 190 mm $\times$ 50 mm openings along two opposing lengths to allow transmission and reception through the polyethylene. The transducer and microphone were affixed to individual 1D motor-controlled positioners aligned to travel across the length of the openings (figure 3)

in order to transmit and receive signals at varying locations along the windows. A diaphragm consisting of two paper layers approximately 0.4 mm in total thickness was placed in the focal plane of the array, to block signals not passing within a few centimeters of the array's geometric center. The primary purpose of this diaphragm was to filter potential artifacts caused by surface modes of vibration induced along the surface and edges of the array. In particular, the outer edge of the acrylic hemisphere generated a signal whose arrival time overlapped with that of the primary signal. This design-induced artifact was fully removed by the diaphragm.

The top of the container remained open to allow the insertion of three acrylic plates ($c = 2750$, m s^{-1} $\rho = 1190$ kg m^{-3}), which were used to assess the ability to measure longitudinal mode phase shifts through the container. Similarly, rod insertions were used in tomographic measurements, as described below in section 2.4.1.

2.4. Imaging demonstrations

2.4.1. Diffraction tomography. A standard assumption for tomographic wave reconstructions is the validity of the first-order Born approximation. However, examining the extreme impedance variation in the media between the transducer surface and the microphone, it must be concluded that the Born approximation—which assumes only first-order scattering—is a particularly poor representation of the present problem. We propose that this failed representation may be overcome by restating the problem: first, the wave transmitted into the tissue phantom will be regarded as a source function. Second, the received wave will be time windowed such that reflections due to the phantom walls are not considered. In this way, the wave field outside of the object is irrelevant to the problem, and the field is regarded in terms of an incident field and internal scatters, such that the pressure reaching a receiver at position $\mathbf{r}_R$ can be written as

$$p(\mathbf{r}_R, \mathbf{r}_S) = p_0(\mathbf{r}_R; \mathbf{r}_S) + \int_{\mathbf{r}'} p_0(\mathbf{r}', \mathbf{r}_S) q(\mathbf{r}') g(\mathbf{r}_R|\mathbf{r}')\, \mathrm{d}^3\mathbf{r}', \tag{1}$$

with $p_0(\mathbf{r}', \mathbf{r}_S)$ describing the incident un-scattered field due to an emitter positioned at $\mathbf{r}_S$. The scattering strength is given by q and within the object and $g(\mathbf{r}_R|\mathbf{r}')$ is the Green's function of the inhomogeneous Helmholtz equation.

The geometry will be deliberately configured to transmit and receive data over parallel lines, such that the source is confined to positions along $z = 0$ and the receiver along $z = Z_R$. If the source aperture is the same regardless of its position $\{X_S 0\}$, the incident field may be written in its Fourier integral form as

$$p_0(\mathbf{r}'; x_S) = \int P_0(k_{S_x})\, \mathrm{e}^{-\mathrm{i}k_{S_x}x_S}\, \mathrm{e}^{\mathrm{i}k_{S_z}z'}\, \mathrm{e}^{\mathrm{i}k'_{S_x}x'}\, \mathrm{d}k'_{S_x}, \tag{2}$$

where the first two terms in the integrand are the Fourier transform of the source function along x separated by the shifting property of the transform. For a point source at $\{X_S,0\}$ the first term reduces to a constant. The third term is the spatial transfer function (projection function) of the transform, where $k_{S_z} = \sqrt{k_0^2 - k_{s_x}^2}$.

Substituting (2) into (1) while further reducing the problem to two dimensions allows the equation to be rewritten as

$$p_s(x_R, x_S)_{Z_R} = \frac{\mathrm{i}}{4\pi} \iint_{k_{S_x}, k_{R_x}} \times \int_{\mathbf{r}'} P_0(k_{S_x})\, \mathrm{e}^{\mathrm{i}k_{S_x}(x'-x_s)}\, \mathrm{e}^{\mathrm{i}k_{S_z}z'} q(\mathbf{r}') \frac{\mathrm{e}^{\mathrm{i}k_{R_x}(x_R-x')}\, \mathrm{e}^{\mathrm{i}k_{R_z}(Z_R-z')}}{k_{R_z}} \mathrm{d}^2\mathbf{r}'\, \mathrm{d}k_{S_x}\, \mathrm{d}k_{R_x}, \tag{3}$$

where the Green's function is written in its integral form under the condition and $Z_R > z'$ and $k_{R_z} = \sqrt{k_0^2 - k_{R_x}^2}$.

Recognizing the inner integral's form as a Fourier integral with respect to x' and z', equation (3) reduces to

$$p_s(x_R, x_S)_{Z_R} = \frac{\mathrm{i}}{4\pi} \iint_{k_{S_x}, k_{R_x}} P_0(k_{S_x}) Q(\mathbf{k}_R - \mathbf{k}_S) \frac{\mathrm{e}^{\mathrm{i}k_{R_z} Z_R}}{k_{R_z}} \mathrm{e}^{\mathrm{i}k_{R_x} x_R} \mathrm{e}^{-\mathrm{i}k_{S_x} x_s} \, \mathrm{d}k_{S_x} \, \mathrm{d}k_{R_x}. \tag{4}$$

Again noting the Fourier form of the integral, it is apparent that equation (4) may be inverted, provided that the function $p_S(x_R, x_S)_{Z_R}$ is known. In practice, this is achieved by measuring over $x_\mathbf{R}$ with the source held stationary. The source is then moved some distance along x_s and the process repeated. The two-dimensional (2D) Fourier transform of this plane leads to the relation needed for reconstruction:

$$P(k_{R_x}, -k_{S_x}) = \mathrm{i} P_0(k_{S_x}) Q(\mathbf{k}_R - \mathbf{k}_S) \frac{\mathrm{e}^{\mathrm{i}k_{R_z} Z_R}}{2k_{R_z}}. \tag{5}$$

Measurements were performed after inserting three wooden rods (3 mm diameter) into the water phantom depicted in figure 3. The rods were fixed in a triangle configuration, 4.8 cm apart and placed normal to the water surface, right-center of the midpoint of the receiver axis, x_R. Based on synthetic 40 kHz data (section 2.1) and reconstruction using equation (5), it was predicted that 11 source points and 11 receiver points each distributed over 160 mm would be adequate for reconstruction.

Data were acquired using the apparatus described in section 2.2.3. A microphone was kept stationary while the focused transducer was moved over 160 mm at a step size of 16 mm. The microphone was then moved to a new position and the process was repeated until the microphone also covered 160 mm at a step size of 16 mm. At each acquisition, eight waveforms were acquired and averaged.

2.4.2. Hand. To demonstrate the ability to measure though tissue *in vivo*, a transmission c-scan of a human hand was performed. While the hand is a poor model for thicker regions of the body, it was selected primarily to overcome limitations of the experimental apparatus. The relative flatness of the hand allowed data to be taken without three-dimensional scanning abilities. In other words, the transducer's focal point and the receiver could both remain close to the skin as the hand was scanned over a 2D grid. The geometry of the hand also allowed for reception of the wave after propagating less than a wavelength through the tissue, thus minimizing diffraction effects and simplifying reconstruction. For practical purposes, the hand could be fixed in a rigid position for the extended period of time (approximately 10 h) that was required for point-by-point data acquisition.

To acquire data, a 2D Cartesian grid was affixed to the diaphragm covering the array. A transparent plastic template of the hand (∼0.2 mm thickness) was marked with crosshairs to allow registered positioning of the hand. A 100 mm × 100 mm opening was cut in the template under the palm of the hand to create an air–skin interface at the transducer focal location. A diagram of the experimental configuration is illustrated in figure 4.

Waveforms were acquired over a 75 mm × 55 mm area with a step size of 2.5 mm across the hand (ulnar border to radial border) and with a step size of 5 mm along the length of the hand, approximately spanning the length of the second, third, and fourth metacarpals. At each position, 40 waveforms were averaged and stored for analysis. The hand was moved to each position manually by sliding the marked plastic template over the surface of the diaphragm.

By only considering the first arriving cycle of the waveform, the thickness of the hand marginally allowed time to analyze the received data without significant contribution from

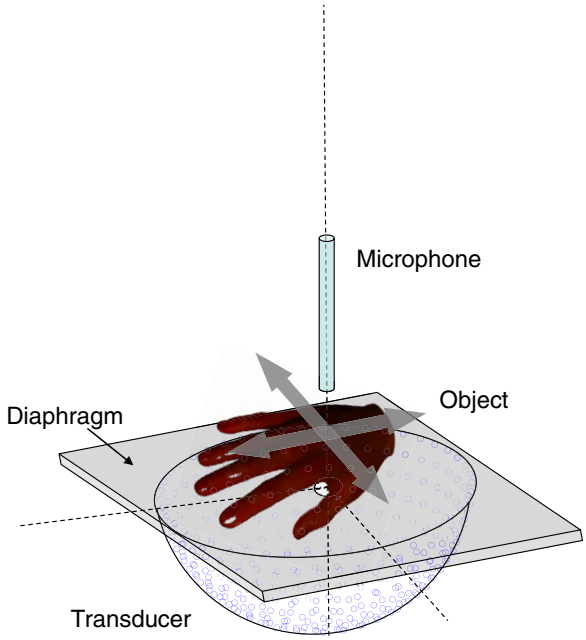

Figure 4. Schematic of the hand scan. The hand was guided over a grid pattern using a guide placed on top of the diaphragm.

multiple reflections. It was predicted that the transmitted amplitude would vary as a function of impedance differences over the beampath, with bone transmitting a lower pressure than softer tissues. Under this assumption reflections within the tissue were neglected. The data were processed by first averaging the 40 acquisitions representing one spatial location and then Fourier transforming the first arriving signal with respect to time. The amplitude of the Fourier transform at the resonant frequency of the transducer (41 kHz) was selected and an image was formed by plotting the values on a base-10 logarithmic scale.

3. Results

3.1. Simulation

After propagating through the 150 mm water layer, the exiting pressure in air was found to be reduced by a factor of 1.3×10^4 at 40 kHz (figure 5(a)) and 3.45×10^4 at 80 kHz (figure 5(b)) relative to the peak focal pressure in air. This reduction represents a power drop by a factor of 1.6×10^8 at 40 kHz and 4.9×10^8 at 80 kHz. These values can be compared with a direct analytical calculation of an incident plane wave, which predicts a pressure drop of approximately 1.3×10^3. In the focused case, the additional order of magnitude drop can be accounted for by wave spreading. Due to the strong reflection at both interfaces of the fluid, the resulting internal waves mask the spherical spreading indicative of a forward-propagating point source (figures 5(a), (b)). This scattering likewise introduced interference in the transmitted wave. These waves are depicted on a magnified intensity scale in figures 5(c) and (d), as their amplitudes are below the intensity resolution of figures 5(a) and (b).

Next, an idealized simulation that neglected internal scattering was performed. This simulation produced a field with spherical spreading of the wave within the fluid resembling

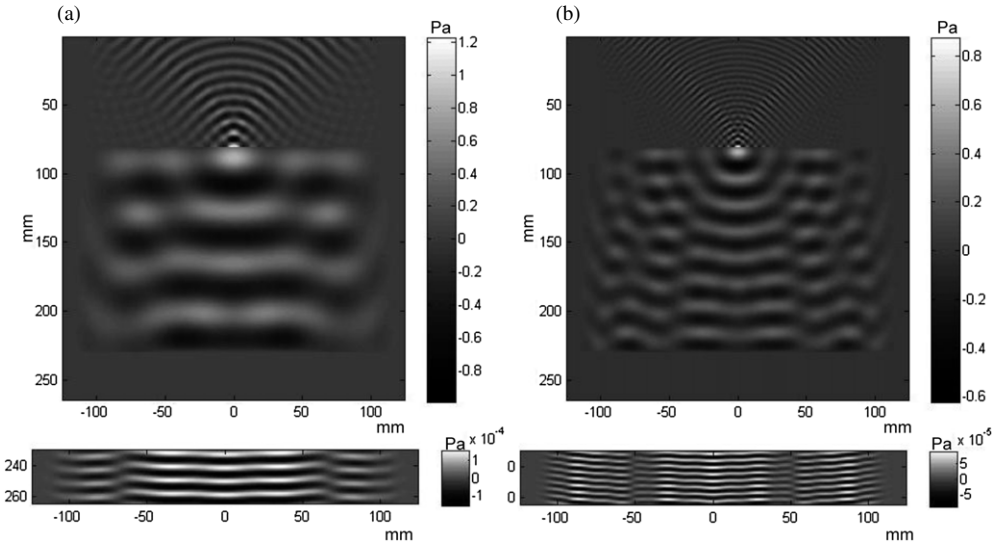

Figure 5. (a) 40 kHz and (b) 80 kHz waves simulated through a tissue layer indicating strong internal scattering.

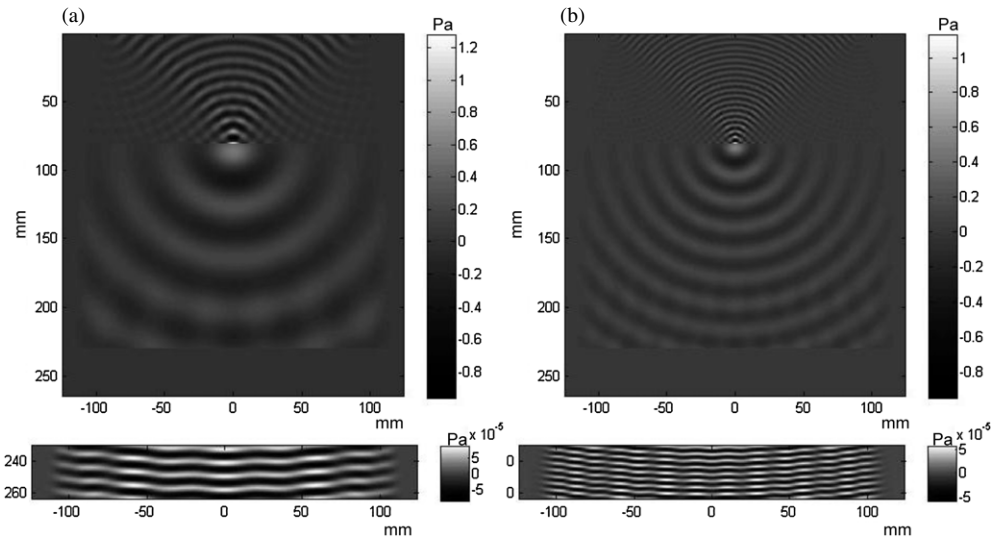

Figure 6. (a) 40 kHz and (b) 80 kHz waves simulated while neglecting scattering. The same phase would be expected in the first arriving waves.

that of a point source (figure 6). This wave pattern would be expected for the first-arriving waves transmitted through the fluid, i.e. until reflected waves had sufficient time to exit the fluid. For the geometries and frequencies used in the current study, this would be restricted to the first 3–4 arriving waveforms. Thus it was determined that analysis would be restricted to the first three arriving wave cycles.

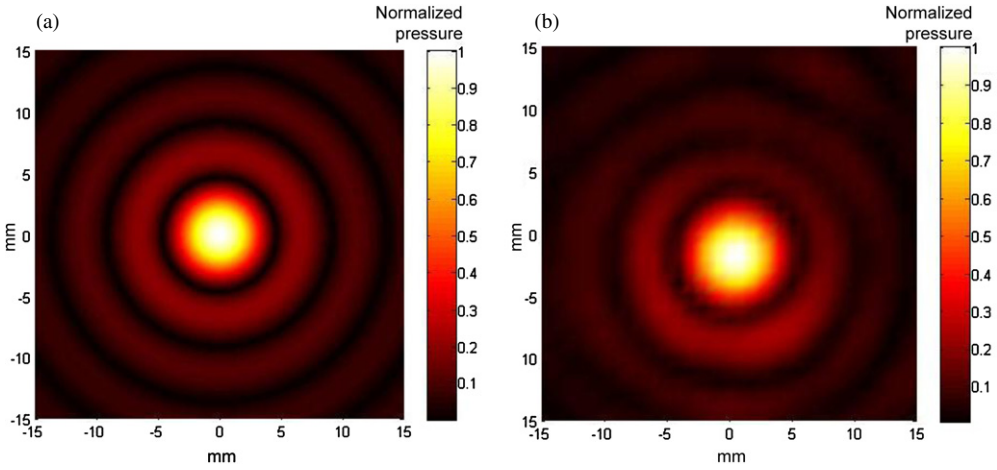

Figure 7. (a) Simulation of the pressure profile at the focal point and (b) the measured result.

3.2. Transducer

For characterization purposes, the field produced by the array when driven by a 20-cycle sinusoidal burst was measured in a plane about its geometrical focus. A beamwidth and sidelobes similar to those predicted numerically were observed (figure 7). The second harmonic of the driving frequency, generated through nonlinear propagation, was found to have a peak amplitude of approximately 30% of the fundamental, and a FWHM focal diameter of approximately 3 mm (figure 8). As the detector radius is on the order of both the signal wavelength and the focal diameter, the exact shape of this signal is regarded as approximate. This is particularly true in regard to sidelobes, which may be underestimated or undetected due to the directionality of the receiver. The complex pressure field over the measurement plane was numerically propagated forward and backward along the axis of symmetry (Clement and Hynynen 2000) to determine radial beam profiles.

Calibrated measurement of the completed array at its focal point showed a peak amplitude of 8.4 kPa (169.5 dB). As this value exceeded the expected, the process was repeated and reconfirmed.

3.3. Transmission measurements

Measurements of pulsed waveforms through water were observed to differ significantly from measurements in air alone. Most pronounced was the extended period of reverberation that, due to the large dynamic range of the receiver, was detectable for over 100 ms after a 5-cycle excitation. As this overall signal contained contributions from multiple longitudinal reflections as well as surface modes of vibration and reflections from within the room it was considered to have little value, and so analysis was restricted to the first 150 μs after first arrival of the waveform. Figure 9 illustrates these differences, showing (a) the measured waveforms at the focus, (b) at the measurement location without the phantom, and (c) with the phantom. The relevant acoustic signal—barely visible on the scale of the reverberation—is shown magnified in (d).

The signal's second harmonic was examined in terms of its amplitude relative to the first harmonic. Due to the transducer's high Q, it was expected that this ratio would rise as a

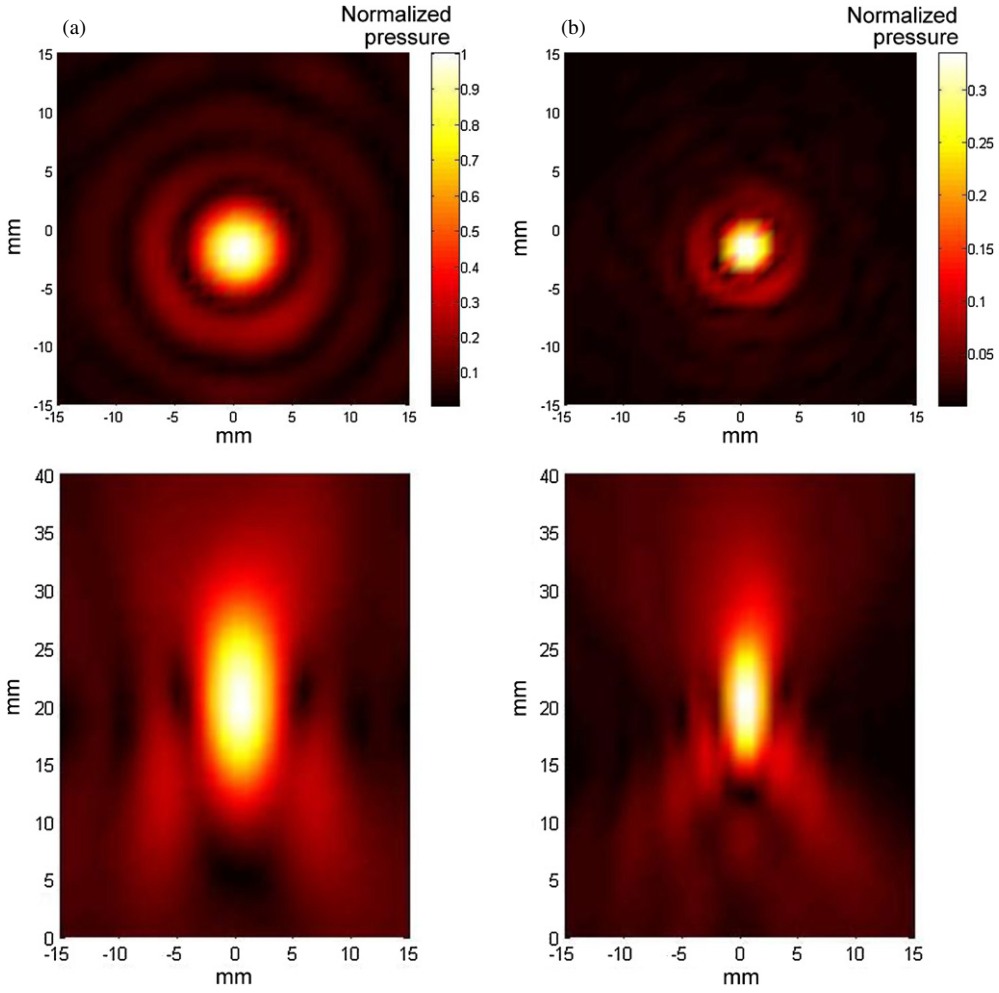

Figure 8. (a) The pressure field of the fundamental frequency at the focus and (b) the nonlinearly generated second harmonic. Projections of the focal plane data toward and away from the transducer provide the axial fields at (a) 40 kHz and (b) 80 kHz.

function of the number of driving cycles. On-axis measurements were acquired at the focus and 150 mm beyond the focus with and without the phantom. Results displayed in figure 10 indicate a relatively close correlation between measurements taken through the phantom and at the focus. In contrast, when measured in air alone this ratio is reduced approximately 30%. The higher ratio through the phantom can be attributed to the point-like spreading in the phantom, which reduces in amplitude approximately inversely with radial distance. Conversely, the second harmonic in air is highly focused, producing a relatively rapid amplitude decay with distance.

Signals were also acquired as three acrylic plates were successively inserted into the tank, forming successively thicker transmission layers. Initial experimentation using 40 signal averages did not produce the expected phase shifts. It was discovered that approximately 400 averages were needed to detect the first three cycles arriving at the microphone, which when analyzed agreed well with expected values (figure 11). When signals beyond the third incoming cycle were evaluated, a systematic phase shift caused by scattering was observed.

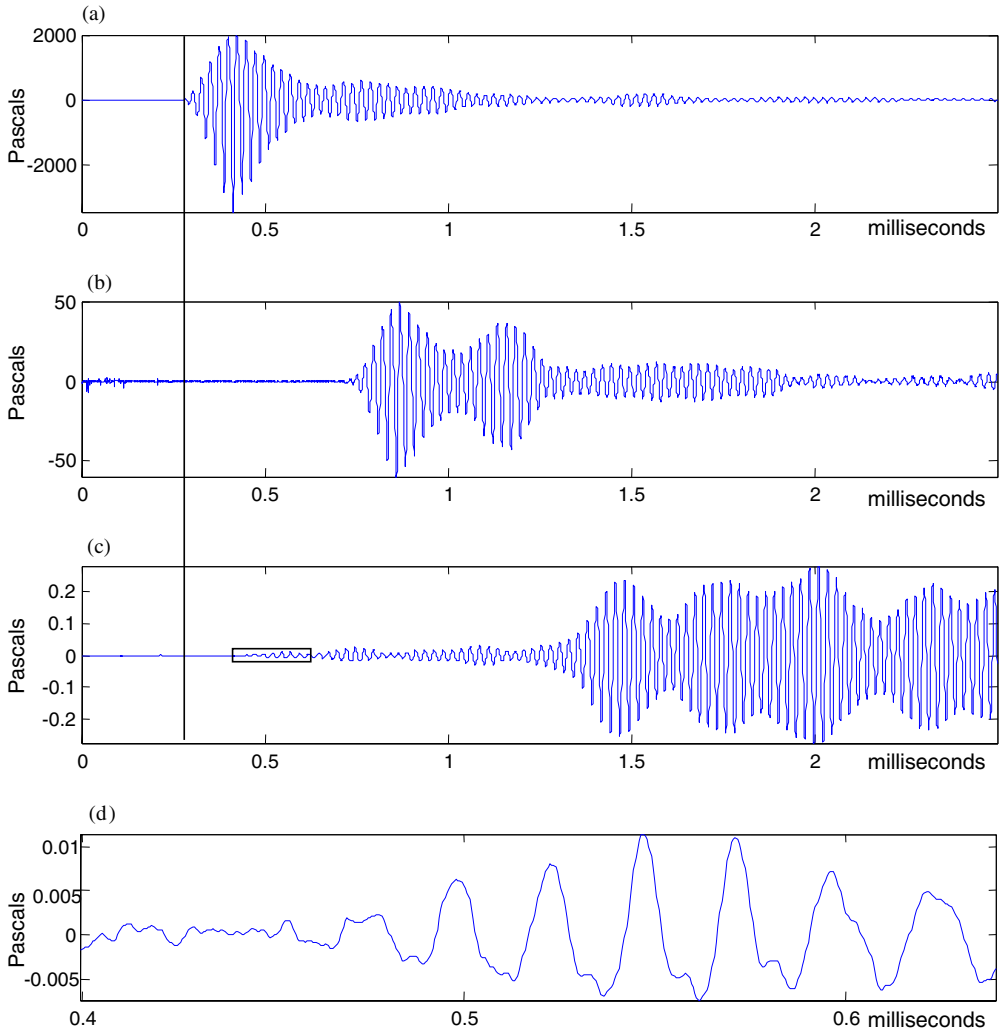

Figure 9. (a) Signal at the focus of the transducer resulting from a 5-cycle sinusoidal burst. (b) The signal along the transducer axis of symmetry at the measurement position depicted in figure 3 before the tank was inserted and (c) the result after passing through the water tank. The initially small waves due to longitudinal propagation are followed by larger amplitude reverberations due to vibration modes on the surface of the phantom. Only the initial signal (d) is used for analysis.

3.4. Imaging demonstrations

The linear tomographic reconstruction was performed using the minimum possible number of acquisitions. While distortion was evident in both the simulated (figures 12(a) and (b)) and experimental data (figure 12(c)), the object positions agreed well with the expected values. Significant artifacts were present in the experimental reconstruction; however, three discernable points can be seen in the image of the 3 mm rods (figure 12(c)).

Distortion and spreading of these points is on the same order of magnitude as that of the simulated case. However, simulation underestimates the scattering strength of one rod, while experimental reconstruction underestimates the strengths of another. We have been unable to

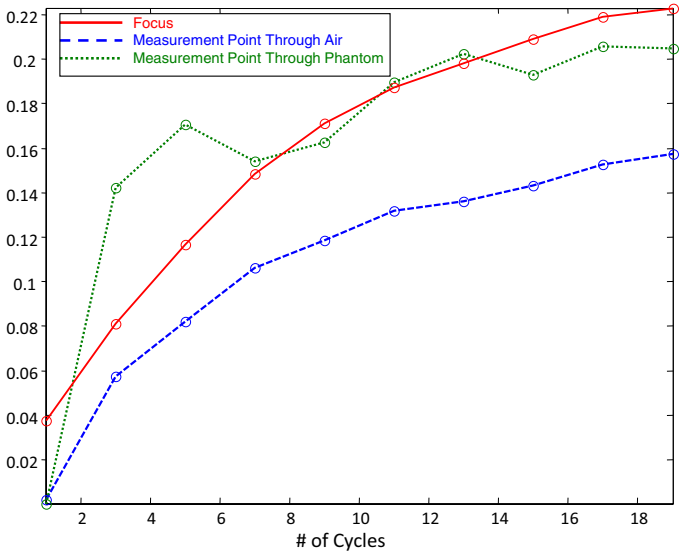

Figure 10. Measurement of the ratios between the second and first harmonic. In air the focused beam diverges faster than the signal through water.

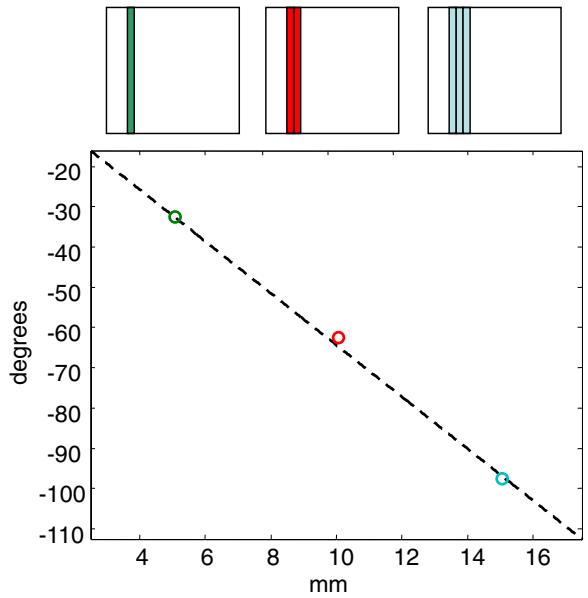

Figure 11. Phase measurements showing phase advance due to 5 mm plates inserted into the water phantom as compared to their expected value (dotted line).

pinpoint the precise reason for this discrepancy; however in both cases it seems to arise from the nonlinear mapping described by equation (5), including the interpolation that is necessary to map using a limited dataset. Increasing k-space resolution is expected to significantly reduce or eliminate these artifacts. Such improvement in the image is evident in simulated data after scaling up the frequency by an order of magnitude (400 kHz).

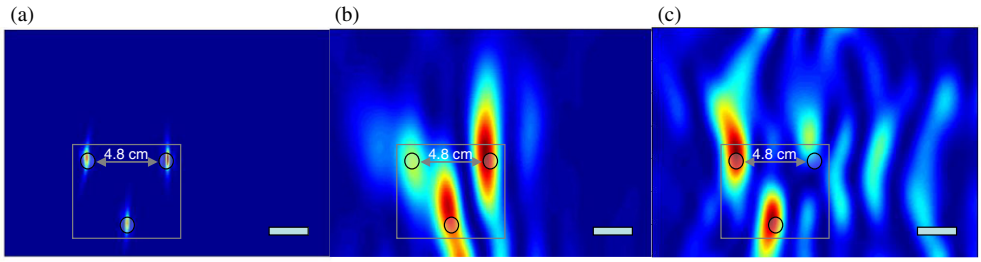

Figure 12. Simulated tomographic reconstructions of three rods placed off center using (a) 400 kHz and (b) 40 kHz. Reconstruction from experimental data is shown in (c).

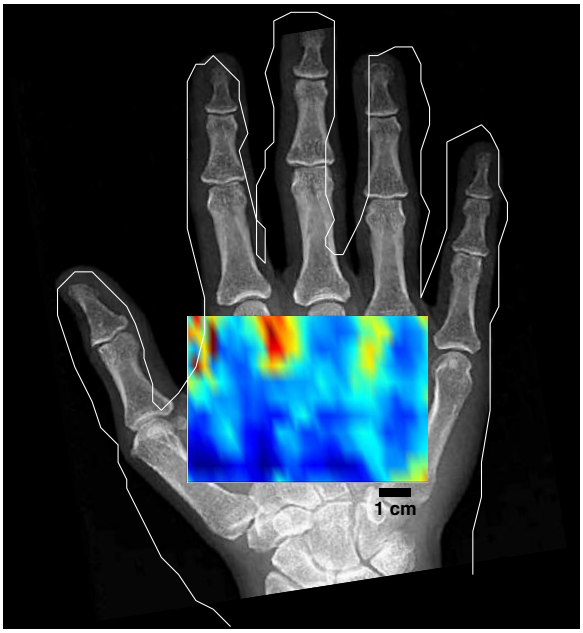

Figure 13. A low-resolution C-mode image of a hand. The background x-ray shows the approximate location of the measurement region relative to the bone anatomy.

A rendering of the first author's hand is shown in figure 13. The image shows a log-scale plot of the contrast difference between areas of tissue alone and those containing bone. The second, third and fourth metacarpals are visible over the ultrasound image. The image is constructed on the assumption that the pressure transmission at a given point is a function of the acoustic impedance in the beampath. Effects of higher order and internal reflections are neglected in this demonstration.

4. Discussion

This study confirms that a point-like ultrasound wave can be introduced into tissue from air and that its exiting waveform can be measured before the arrival of internal scattering and external wave modes. The point-like shape of the wave is significant, as it indicates a potential source for fan-beam tomographic reconstruction. Reception of the first arriving longitudinal

waves is also important, as these waves contain phase information unaltered by boundary reflection. One fortunate acoustic property is the relatively fast speed of the longitudinal waves in water (as well as tissues) as compared to surface modes of vibration. In the present work, clear detection of purely longitudinal was possible, but required signal averaging between 40 iterations through water to 400 iterations through both water and acrylic plates. Overall, results suggest that tomographic-based non-contact imaging is feasible.

The array studied here was designed to demonstrate feasibility, with design constraints largely based on cost and practical construction. A larger, higher frequency array would improve signal strength, resolution, and the number of cycles that could be acquired before the arrival of multiple reflections.

Implementation of a large area reconstruction (Devaney 1985) would likely require that both forward and backscattered data is received from the body. For rapid acquisition this will necessitate an array of detectors, or an alternative means of recording vibrations at a specific location (e.g. laser measurement). A method of registering the receiver and detector's position relative to the points of focusing and measurement on the body is also necessary to perform reconstruction. Even with these added acquisition and registration abilities, image formation would not be trivial. Existing methods for arbitrary diffraction tomography (Devaney and Beylkin 1984), despite their generality, still rely on assumptions of slowly varying curvature relative to the wavelength, something that cannot be assumed in the present problem. Reconstruction is mathematically possible, but only if both the scattered wave and its normal derivative can be determined over the measurement surface (Devaney and Beylkin 1984). Our ongoing efforts are concentrating on developing such an algorithm.

Resolution will ultimately be constrained by the increased absorption of ultrasound in air at higher frequencies. At the current driving frequency and its second harmonic the pressure loss due to absorption over the 90 mm focal distance is expected to only be a few per cent. By increasing the driving frequency one order of magnitude, a loss of 25% would be expected at 400 kHz ($\alpha \sim 3$ Np m^{-1}) and over 50% at 800 kHz ($\alpha \sim 9$ Np m^{-1}). This loss would approach 90% by 1 MHz ($\alpha \sim 23$ Np m^{-1}). However, at 800 kHz this would allow for image resolution of slightly below 1 mm, which would be of value to medical diagnostics.

While the frequency of 40 kHz used for this feasibility study was understood to be suboptimal for imaging, generalized diffraction tomography showed that linear targets, and hence the small signals resulting from scattering could be detected. In future operation, reconstructions will likely concentrate on phase imaging induced by sound speed variation in tissue. Practical implementation will require a higher frequency transducer and methods of fast signal reception over a closed curve around the body. Optical vibrometry may be one possible means of meeting these criteria. Even with a fast acquisition method, the approach still presents a mathematical challenge: The data will be acquired over an irregular (non-separable) shape, namely the body surface. Current efforts are focused on solving this inverse problem. Despite these challenges, the results of this feasibility study are encouraging, having confirmed the ability to create and detect a point-like ultrasound source without contact.

Acknowledgment

This work was supported by The University of Electro-Communications Center for Industrial and Governmental Relations.

References

Berriman J, Purnell P, Hutchins D A and Neild A 2005 Humidity and aggregate content correction factors for air-coupled ultrasonic evaluation of concrete *Ultrasonics* **43** 211–7

Bulman J B, Ganezer K S, Halcrow P W and Neeson I 2012 Noncontact ultrasound imaging applied to cortical bone phantoms *Med. Phys.* **39** 3124–33

Clement G T and Hynynen K 2000 Field characterization of therapeutic ultrasound phased arrays through forward and backward planar projection *J. Acoust. Soc. Am.* **108** 441–6

Devaney A J 1982 A filtered backpropagation algorithm for diffraction tomography *Ultrason. Imaging* **4** 336–50

Devaney A J 1985 Generalized projection-slice theorem for fan beam diffraction tomography *Ultrason. Imaging* **7** 264–75

Devaney A J and Beylkin G 1984 Diffraction tomography using arbitrary transmitter and receiver surfaces *Ultrason. Imaging* **6** 181–93

Gan T, Hutchins D and Billson D 2002 Preliminary studies of a novel air-coupled ultrasonic inspection system for food containers *J. Food Eng.* **53** 315–23

Gan T H, Hutchins D A, Billson D R and Schindel D W 2001 The use of broadband acoustic transducers and pulse-compression techniques for air-coupled ultrasonic imaging *Ultrasonics* **39** 181–94

Hall K S 2011 Air-coupled ultrasonic tomographic imaging of concrete elements *PhD Dissertation* University of Illinois, IL, USA (available at: http://hdl.handle.net/2142/26142)

Iraniha S, Cinat M E, VanderKam V M, Boyko A, Lee D, Jones J and Achauer B M 2000 Determination of burn depth with noncontact ultrasonography *J. Burn Care Rehabil.* **21** 333–8

Jing Y, Tao M and Clement G T 2011 Evaluation of a wave-vector-frequency-domain method for nonlinear wave propagation *J. Acoust. Soc. Am.* **129** 32–46

Jing Y, Wang T and Clement G 2012 A k-space method for moderately nonlinear wave propagation *IEEE Trans. Ultrason. Ferroelectr. Freq. Control* **59** 1664–73

Treeby B E, Jaros J, Rendell A P and Cox B T 2012 Modeling nonlinear ultrasound propagation in heterogeneous media with power law absorption using a k-space pseudospectral method *J. Acoust. Soc. Am.* **131** 4324–6